

The Cause of Internal Outflow Surges in a High-Resolution Simulation of the 8 May 2003 Oklahoma City Tornadic Supercell

Alexander D. Schenkman¹, Ming Xue^{1,2}, and Daniel T. Dawson II^{1,3}

Center for Analysis and Prediction of Storms¹ and School of Meteorology²
University of Oklahoma, Norman Oklahoma 73072

Department of Earth, Atmospheric, and Planetary Sciences³
Purdue University, West Lafayette, Indiana

Submitted April 2015

Revised: July 2015

Accepted September 2015

Journal of Atmospheric Sciences

Corresponding author address:

Alexander D. Schenkman

Center for Analysis and Prediction of Storms

University of Oklahoma,

120 David L. Boren Blvd, Norman OK 73072

alex3238@ou.edu

Abstract

A high-resolution simulation of the 8 May 2003 Oklahoma tornadic supercell is analyzed to determine the origin of internal outflow surges within the low-level cold pool. The analyzed simulation has 50-m horizontal grid spacing and is quadruply nested within larger, lower resolution domains that were initialized via 3DVAR data assimilation of radar and other observations. The high-resolution simulation produces two tornadoes that track in close proximity to the observed tornado on 8 May 2003. Our previous study determined that an internal outflow surge instigated tornadogenesis for the first tornado in this simulation but the cause of this internal outflow surge was unclear.

In this study, the vertical momentum equation is analyzed along backward trajectories that are initialized within the tornado-triggering internal outflow surge. The analysis reveals that the internal outflow surge is forced by the dynamic part of the vertical pressure gradient. Further examination reveals that the dynamic forcing is the result of a high-pressure perturbation in an area of stagnating flow on the west and northwest side of the low-level (below ~3 km AGL) mesocyclone. This region of high perturbation pressure is unsteady and forces several other warm internal outflow surges on the west side of the tornado. Cold internal outflow surges also occur later in the simulation and are shown to be buoyantly forced by evaporation and water loading in heavy precipitation.

1. Introduction

One of the most recent significant findings in tornadic supercell research has been the presence of internal outflow surges behind the primary rear-flank gust front (RFGF). The most important advancement that has led to the identification of these surges has been the development of mobile Doppler radars (e.g., Wurman et al. 1997; Biggerstaff et al. 2005; Bluestein et al. 2010; Pazmany et al. 2013). These radars typically have much higher spatio-temporal resolutions than operational radars (e.g., WSR-88D and TDWR) and their mobile nature have allowed for the collection of data sets that are in close proximity to supercells. Researchers that have examined these data sets have found that internal outflow surges are common behind the primary RFGF (Wurman et al. 2007b, a; Marquis et al. 2008; Wurman et al. 2010; Skinner et al. 2011; Marquis et al. 2012; Kosiba et al. 2013; Skinner et al. 2014). Because the discovery of these surges is relatively recent, more quantitative knowledge of their frequency of occurrence is still unknown. However, recent coordinated efforts between mobile surface observations (e.g., mobile mesonets and sticknets) and mobile Doppler radar have provided a look at the thermodynamic and kinematic structure of internal outflow surges (e.g., Skinner et al. 2011; Lee et al. 2012; Skinner et al. 2014).

Mobile mesonet data collection has provided valuable insight into the near-surface thermodynamic properties of internal outflow surges (Finley and Lee 2008; Hirth et al. 2008; Finley et al. 2010; Lee et al. 2011; Lee et al. 2012). Hirth et al. (2008) found that the RFD outflow in one of the supercells they studied was comprised of transient thermodynamic features with very warm regions of air present behind the RFGF. The internal outflow surge in this case was generally warmer than the surrounding RFD outflow. Lee et al. (2011) also found a warm internal outflow surge in the supercell they studied. However, data presented in Finley et al. (2010) and Lee et al. (2012) suggest the thermodynamic properties of internal outflow surges may vary dramatically within a single storm. They analyzed mobile mesonet data from a strongly tornadic supercell and found four internal outflow surges all with different thermodynamic properties during a single low-level mesocyclone occlusion cycle. Warm surges were generally present during times of tornadogenesis and intensification, whereas, cold surges were coincident with tornado weakening and dissipation.

A connection between internal outflow surges and tornado maintenance has been proposed by Marquis et al. (2012). Through dual-Doppler and ensemble Kalman Filter (EnKF) analyses of four supercells they concluded that internal outflow surges help to generate and maintain tornadoes through enhanced convergence and baroclinic vorticity generation. They reached the latter conclusion by noting the presence of vortex line arches (Straka et al. 2007; Markowski et al. 2008) over the internal gust front. A relationship between tornadoes and internal outflow surges has also been suggested by Finley et al. (2010), Lee et al. (2011,2012), and Kosiba et al. (2013), with Kosiba et al. (2013) proposing that enhanced convergence associated with an internal outflow surge was responsible for tornadogenesis via increased tilting and stretching of vertical vorticity.

Although observational studies are able to capture some of the kinematic and near-surface thermodynamic structures of internal outflow surges, their ability to determine the dynamical processes responsible for the surges is limited by restricted low-level radar beam coverage (due to earth curvature and the minimum elevation of the radar beam) and limited spatio-temporal coverage of the mobile mesonets (observations are only available along roads and at the surface). In lieu of observational data, a numerical modeling approach can be used to diagnose the dynamics of internal outflow surges in simulated storms. Adlerman (2003) noted a secondary RFD surge in one of his simulations but did not analyze its properties or origin in depth. Mashiko et al. (2009) modeled a tornadic mini-supercell that occurred in association with a landfalling typhoon. Via

sensitivity experiments, Mashiko et al. (2009) suggested that an internal outflow surge was responsible for tornadogenesis in their simulations. Moreover, their study finds that the downdraft leading to this internal outflow surge was the result of enhanced water loading as a simulation with water loading turned off did not produce an internal outflow surge.

In the present study, we adopt the numerical modeling approach to examine the origin and dynamics of internal outflow surges in a high-resolution simulation of the 8 May 2003 OKC tornadic supercell. Tornadogenesis in this simulation was investigated in Schenkman et al. (2014); hereafter SXH14. They found that surface drag played an important role in the generation of low-level horizontal vorticity that was re-arranged into the vertical in association with tornadogenesis. In addition, SXH14 found that tornadogenesis was preceded by an internal outflow surge in their simulation. The cause of the internal outflow surge was speculated to be the result of water loading given the thermodynamic properties of the surge. However, the origin of internal outflow surges was tangential to the main goal of SXH14 and as such was not examined in detail.

Given the importance of internal outflow surges found in SXH14, Mashiko et al. (2009), as well as in many observational studies, we examine in this paper the dynamics behind the momentum surges in the simulation of SXH14. More specifically, the focus is on the momentum forcing rather than the vorticity dynamics that was examined in SXH14.

The remainder of the paper is organized as follows: Section 2 briefly presents the 8 May 2003 case and reviews the simulation experiment design and main findings of SXH14. Section 3 describes a pressure decomposition used to examine the momentum forcing for downdrafts responsible for the internal outflow surges. Section 4 discusses the evolution and origin of multiple internal outflow surges. A summary and conclusions are presented in section 5.

2. Methodology

a. The 8 May 2003 OKC tornadic Supercell

On 8 May 2003, an F-4 tornado struck the south side of the Oklahoma City metropolitan area. The parent supercell was initiated around 2100 UTC along a dryline in central Oklahoma in an environment with $> 3800 \text{ J kg}^{-1}$ of mixed-layer CAPE and storm-relative environmental helicity of $> 450 \text{ m}^2 \text{ s}^{-2}$. The storm produced two weak, short-lived tornadoes just southwest of Moore, Oklahoma between 2200 and 2208 UTC. At 2210 UTC, a much stronger tornado formed on the west side of Moore and produced damage of up to F-4 intensity along its 27-km track. The tornado dissipated at 2238 UTC and the OKC supercell then began to weaken, dissipating around 0000 UTC 9 May 2003. A more detailed discussion of the 8 May 2003 OKC supercell can be found in Hu and Xue (2007), Romine et al. (2008), Xue et al. (2014), and SXH14.

b. Overview of Schenkman et al. (2014)

SXH14 examined a high-resolution simulation of the 8 May 2003 OKC supercell reported in Xue et al (2014). This simulation was conducted with a quadruply nested grid. The innermost nest had 50-m horizontal grid spacing. The 50-m simulation started from a 20-min simulation valid at 2200 UTC on the 100-m grid. The 100-m grid itself was initialized from an interpolated final analysis on a 1-km grid valid at 2140 UTC after 70 min of cycled data assimilation – see Fig. 3 of Xue et al. 2014. The simulation used single-moment Lin-type ice microphysics (Lin et al. 1983; Tao and Simpson 1993), with Lin 3-ice microphysics and the rain intercept value set at the default value of $8 \times 10^6 \text{ m}^{-4}$. Two tornadoes formed in close proximity to the observed tornado during the 40-min forecast that was run on the innermost nest. The stronger of the two tornadoes reached F-4 intensity (based on maximum wind speed at the lowest model level) and persisted for

13 min. Fig. 1 (adapted from SXH14) presents an overview of the simulated supercell on the 50-m grid spacing domain. More details of the experiment design and simulation results on the lower-resolution domains can be found in Xue et al (2014) and SXH14.

SXH14 conducted backward trajectory analyses on the 50-m grid to determine the origin of vertical vorticity for both simulated tornadoes. Notably, their analysis revealed that horizontal vorticity generated by surface drag played an important role in the development of pre-tornadic vorticity in several areas. An internal outflow surge was suggested to have triggered tornadogenesis via increased low-level convergence and additional enhancement of low-level frictionally generated horizontal vorticity. SXH14 speculated that the internal outflow surge was driven by water loading because it was relatively warm and associated with a reflectivity maximum. However, they did not analyze in depth the actual cause of the surge or its relation to the tornado.

3. Vertical momentum diagnostic solver

In this section, we describe the pressure decomposition used to examine the momentum forcing for downdrafts responsible for the internal outflow surges. This decomposition is conducted as follows: After splitting the total pressure perturbation p' into a *dynamic component* p_d' associated solely with variations in the flow (i.e., as might be manifested in vorticity and deformation fields) and a *buoyant component* p_b' associated solely with density variations, the anelastic vertical momentum equation can be written in Lagrangian form as

$$\frac{Dw}{Dt} = -\frac{1}{\bar{\rho}} \frac{\partial p_d'}{\partial z} + \left(-\frac{1}{\bar{\rho}} \frac{\partial p_b'}{\partial z} + B \right) + F, \quad (1)$$

where $\bar{\rho}$ is the horizontally-homogeneous base state air density, B is the standard buoyancy given by $B \equiv g \rho' / \bar{\rho}$, F is the frictional force, and all other symbols have their standard definition. As discussed by Emanuel (1994), Davies-Jones (2003), and Doswell and Markowski (2004), by separating the total pressure perturbation p' in this manner, one arrives at a *base-state independent* formulation of the “buoyant contribution”, which is the sum of the two terms in () on the RHS of (1). This term contains the effects of both the standard (or Archimedean) buoyancy B and that of the perturbation pressure field directly instigated by B . The first term on the RHS of (1) is the *dynamic* vertical perturbation pressure gradient force (DVPPGF) due solely to variations in the flow field. Together these terms make up the static and dynamic parts of the locally-nonhydrostatic vertical pressure gradient force (NHVPGF) responsible for vertical accelerations (Davies-Jones 2003).

Davies-Jones (2003) derived a formula for the static part of the NHVPGF that can be computed directly from the density field:

$$-\nabla^2 \beta = g \nabla_H^2 \rho_T, \quad (2)$$

where ∇^2 and ∇_H^2 are the 3D and horizontal Laplacian operators, respectively, β is the “effective buoyancy” (which is equivalent to the “buoyant contribution” described previously), g is the acceleration due to gravity, and ρ_T is the total *system density* which includes the density of moist air plus suspended hydrometeors (Davies-Jones 2003).

To produce analyses of β and DVPPGF for this study we solve (2) utilizing the multi-grid solver *mud3cr* available in MUDPACK (Adams 1989) on an appropriate 3D subdomain of the 50-m grid. We then compute DVPPGF as a residual from the known model instantaneous Lagrangian

vertical acceleration field (minus the friction and Coriolis terms, which are both very small—see below). Additionally, we separately compute the part of β due *only* to hydrometeor loading β_q by recognizing the linearity of the Laplacian operators in (2) and computing the difference between the effective buoyancy in (2) from that using the total moist air density *without* the contribution from hydrometeors ρ (Davies-Jones 2003). Therefore, we have:

$$-\nabla^2 \beta_q = g \nabla_H^2 (\rho_T - \rho). \quad (3)$$

By computing total effective buoyancy β and hydrometeor loading contribution β_q instead of the more traditional “standard” buoyancy B (and its components), we avoid the ambiguities and potential misleading physical interpretations that inevitably arise from the arbitrary choice of a base state, as well as implicitly include the spatially extended effects of the buoyancy via the instigated perturbation pressure field (as encapsulated by p_b).

After Davies-Jones (2003), we impose the homogeneous Dirichlet condition $\beta = 0$ on the bottom boundary. While this choice of bottom boundary condition has been made by Davies-Jones (2003) and others under the assumption that not only the total vertical acceleration, but also its components (i.e. β and DVPPGF), should vanish at flat ground, until recently no rigorous justification of this assumption has been attempted. Jeevanjee and Romps (2015) have shown with their novel (but equivalent) definition of β , that this condition is in fact the unambiguously correct one for a flat bottom boundary. Here, we also impose this condition for the effective water loading β_q . We also set the top and lateral boundary conditions to homogeneous Dirichlet for faster convergence as testing (not shown) confirmed that the interior solution was insensitive to the choice of Neumann or Dirichlet conditions for these boundaries. Further details can be found in Dawson et al. (2015).

4. Simulation results and the origin of internal outflow surges

We first discuss the overall evolution of the simulation with particular attention to internal outflow surges. Internal outflow surge locations are subjectively determined based on animations of perturbation virtual potential temperature (θ_v') and wind vectors (not shown). Specifically, we inspect these animations to find the leading edge of enhanced momentum and θ_v' gradients. From these animations several areas of surging outflow that move toward the primary RFGF are readily apparent. In this section, we first focus on the tornado-triggering internal outflow surge discussed in SXH14.

a. Overview of internal outflow surges in the simulated OKC supercell

The interpolated initial condition of the 50-m grid-spacing domain features a classic supercell with high simulated radar reflectivity factor over the northwest part of the model grid (Fig. 1a). In association with this supercell, a large cold pool is present over much of the western half of the 50-m grid-spacing domain (Fig. 2a). There are many pockets of relatively high and low θ_v' (hereafter referred to as warm and cool/cold) within the cold pool. Over the first 360 s of the 50-m simulation, a well-defined RFGF develops in the southwest portion of the supercell (Fig. 2b). The air behind the RFGF is relatively cool ($\theta_v' \sim -3$ to -6 K). A forward-flank convergence boundary (FFCB, e.g., Beck et al. 2006; Beck and Weiss 2013) marks the leading edge of rain-cooled air in the forward flank of the storm and extends to the northeast from the RFGF. The cold pool is still fairly heterogeneous with several warm pockets of air well to the rear of the RFGF and FFCB (Fig. 2b). An internal outflow surge is evident behind the primary RFGF (Fig. 2b). This

internal outflow surge was warm upon formation and by 2207 UTC (Fig. 3a) has cooled to temperatures similar to that of the rest of the air behind the primary RFGF.

The tornado-triggering internal outflow surge discussed in SXH14 becomes apparent near the ground around 2208 UTC (Fig. 3b). θ_v' is initially a couple of K higher than the surrounding outflow air. The tornado-triggering internal outflow surge races to the southeast (Fig. 3b-c), and nears the pre-tornadic vortex (PTV) by 2210 UTC (Fig. 3d). After tornadogenesis, the tornado-triggering internal outflow surge becomes difficult to distinguish from the initial internal outflow surge and the outflow takes on a more steady temperature configuration with cool air from both the forward flank and rear-flank wrapped around the tornado (Fig. 4a). A large area of relatively warm outflow air is wrapped around the outside of the cool outflow air (Fig. 4a,b). The origin of this warm air will be examined in more detail in the following section.

The cold inner/warm outer configuration of the outflow around the tornado persists until around 2222 UTC when the tornado begins to weaken and is surrounded by increasingly cool outflow (Fig. 5). Around 2225 UTC, the tornado dissipates with a strong central downdraft leaving behind a pocket of relatively warm air (Fig. 5b). As the first tornado weakens, a second tornado forms to the northeast of the first tornado (Fig. 5a). This new tornado forms along the primary RFGF which by this time has progressed about 10 km to the east of the first tornado. As described in SXH14, the second tornado formed as an area of weak downdraft associated with a developing convective cell to the east of the RFGF moved to the north-northwest and intersected the primary RFGF. The outflow/cold pool structure associated with the second tornado is less complex than that associated with tornado 1. With time, increasingly cool outflow wraps around tornado 2 (Fig. 5b). The second tornado dissipates around 2228 UTC.

b. Trajectory analysis and vertical momentum forcing for the tornado-triggering internal outflow surge

We now diagnose the vertical momentum forcing as described in section 3. These forcing terms are calculated on the model grid and interpolated to points along backward trajectories that were initialized every 20 seconds on an 8x8 km grid at 20-m AGL with 100-m spacing surrounding the first tornado. The trajectories are integrated backward until the beginning of the 50-m simulation. Two-second model output data are used to calculate the backward trajectory positions. To further increase trajectory position accuracy, a 0.2-s sub interval is used in which winds from the output times are linearly interpolated (Dahl et al. 2012).

Fig. 6 marks the locations of parcels at 2210 UTC that subsequently enter the tornado between 2210 and 2215 UTC and reveals a clustering of parcels within the northern half of the tornado-triggering internal outflow surge. In order to be considered a tornado parcel, a parcel must attain a wind speed exceeding 32 m s^{-1} and a vertical vorticity $> 0.1 \text{ s}^{-1}$ while below 250 m AGL. The height criterion is used to eliminate parcels that enter the low-level mesocyclone but not the tornado. Sensitivity tests of the above criteria showed that the number of parcels, but not the areas they originated, was impacted by increasing/decreasing the wind and vorticity criteria (not shown). Note that parcels within and immediately adjacent to the PTV in Fig. 6 are not flagged as tornado-parcels because they pass through the PTV before it reaches tornadic intensity (i.e., the wind speed criterion is not met).

We now focus on parcel trajectories that are within the tornado-triggering internal outflow surge (Fig. 6). Parcels within this surge follow two distinct paths: (I) The majority of parcels come from the west starting their descent into the internal outflow surge around $\sim 1.5\text{-}2.5$ km AGL. (II) Other parcels originate in the inflow at around 0.75-1.0 km AGL. These parcels descend more gradually as they pass through the forward flank of the storm.

Fig. 7a presents the forcing along the trajectory¹ for a representative parcel from trajectory path (I). The general evolution of the forcing along the chosen trajectory is representative of the forcing along all the parcels that follow path (I). It is clearly seen that the DVPPGF dominates the vertical momentum equation. The parcel is first dynamically forced upward between 2201-2204 UTC. More important for internal outflow surge formation, the parcel is subsequently dynamically forced downward from 2204-2207 UTC causing rapid descent. The parcel briefly ascends between 2208 and 2209 UTC before resuming its descent and nears the surface in the surge around 2210 UTC. Forcing terms for a parcel that follows trajectory path (II) in the internal outflow surge are shown in Fig. 7b. Between 2204 and 2206 UTC, negative effective buoyancy dominates the vertical momentum forcing for these parcels. After 2206 UTC, dynamic forcing slows the descent of the parcel and then leads to a brief period of ascent. This brief period of ascent is followed by descent back to the near-surface.

It is worth making a brief comment regarding the effective water loading term β_q . It may be seen that this term is occasionally positive along the trajectories in Fig. 7 and subsequent similar figures (dashed green lines). This initially counter-intuitive result is because β_q contains contributions from both the traditional water loading (which is always negative in regions of positive hydrometeor content, and always zero elsewhere) *and* the (non-dynamic) VPPGF induced by the water loading (c.f. term in parentheses in Eqn. 1). For example, in regions adjacent to precipitation shafts, there is often a compensating upward-directed (positive) VPPGF directly associated with the presence of the precipitation shaft (not shown).

In order to determine which parcel trajectory is more important to internal outflow surge formation, we examine parcel trajectories in and around the surge at earlier times. Fig. 8 shows that at 2209 UTC parcels that are adjacent to the internal outflow surge all follow path (II). In contrast, parcels within the internal outflow surge all follow path (I). Additionally, parcels that follow path (I) descend much more rapidly and have greater momentum than those in path (II). As such, it stands to reason that the parcels that follow path (II) are not important players in the formation of the internal outflow surge but are merely entrained into the surge as it moves to the southeast.

While the above analysis shows that internal outflow surge is generated primarily via the DVPPGF, it does not provide a physical explanation of the surge with respect to key storm features. Namely, we seek to investigate what processes in the storm are causing the internal outflow surge to develop. Given the primarily dynamic forcing mechanism for the surge described above, we examine the pressure field around the low-level mesocyclone (below ~ 3 km AGL).

Fig. 9 shows a relative maximum of perturbation pressure on the far north-northwest side of the mesocyclone at 2205 UTC (Fig. 9). This area of relative high pressure is within a stagnation zone where the southeasterly flow associated with the low-level mesocyclone encounters the westerly flow associated with the environmental flow. Parcels from path (I) are all located beneath this pressure enhancement as they begin their rapid descent (Fig. 9). Plots of DVPPGF confirm that these parcels are within relatively strong downward forcing at this time (Fig. 10). The relative maximum in perturbation pressure is short-lived, persisting for only about 3 min (not shown), which helps to explain why the surge is limited in time and space and hence rather transient.

The above analysis reveals the origin and forcing mechanism responsible for the internal outflow surge; it does not, however, explain the cause of the rapid fluctuation of the pressure field

¹ In Fig. 7 (and subsequent) plots of the forcing along representative trajectories, the friction term in equation (1) is not plotted because it was near zero throughout the period examined.

that leads to the downward vertical pressure gradient. In other words, it is unclear why the pressure maximum develops and dissipates in about 3 min. Unfortunately, a full explanation of this fluctuation is difficult owing to the tremendous complexity and non-linearity in such high resolution simulations as well as the non-steadiness of the overall simulated storm. Dynamic pressure perturbations are by definition associated with changes in the flow field and therefore rapid changes in the flow structure in this region will result in rapid pressure fluctuations. We speculate that the behavior of the pressure maximum is most likely related to unsteadiness in the supercell's updraft and low-level mesocyclone (which in turn would modulate the intensity of southeasterly flow 2-3 km AGL) combined with heterogeneity in the environmental flow to the rear of the supercell. Confirming or disproving such speculations would require separate studies, including carefully designed idealized experiments; these are beyond the scope of the present study, which focuses on the direct forcing of the internal outflow surges.

c. The origin of warm air on the outer flank of the hook echo.

As mentioned above, in the minutes leading up to and after tornadogenesis the outflow takes on a configuration with a warm band of air wrapped around the cooler outflow that envelops the simulated tornado. In this subsection, we examine the origin of this warm outflow air using trajectory analysis and examining the vertical momentum forcing terms.

Vertical momentum forcing terms along backward trajectories from the warm curtain of air surrounding the tornado (Fig. 11) reveal that these parcels are predominantly dynamically forced downward. These parcels come mainly from the southwest and southeast (Fig. 11). Forcing terms along a representative parcel from the southwest are shown in Fig. 12a. It is clear that the DVPPGF dominates the vertical excursions of the parcel. The effective buoyancy force is generally upward as a result of the parcel's warmth relative to the surrounding environment. The effective water loading term remains near zero, which is (for example) consistent with the parcel 1) being relatively precipitation free and somewhat removed from areas of substantial precipitation, 2) being embedded in a locally relatively homogeneous area of precipitation, or 3) being embedded in a region of relatively light precipitation located near relatively heavier precipitation. A check along the parcel trajectory confirms that the parcel is in light precipitation just to the rear of the heavier precipitation of the hook echo throughout its path (not shown). Towards the end of the trajectory the dynamic forcing becomes positive, decelerating the parcel as it approaches the ground.

In contrast to the trajectory from the southwest, forcing terms along a representative trajectory from the southeast (Fig. 12b) show that effective buoyancy plays some role in the descent of the parcel. Specifically, the parcel becomes negatively buoyant as it rotates around the low-level mesocyclone and passes through the storm's precipitation core. As the parcel continues to descend the effective buoyancy forcing reverses sign owing to the relative warmth of the parcel. However, the parcel continues to descend rapidly because the downward DVPPGF remains large. This suggests that the DVPPGF is playing the principal role in forcing the descent of this air parcel to the near-surface. As with the parcel from the southwest, dynamic forcing becomes positive as the parcel approaches the lower boundary of the model.

Examination of the pressure perturbation at 1.5 km AGL (Fig. 13a) reveals an area of high pressure on the southwest side of the low-level mesocyclone. As with the tornado-triggering internal outflow surge, this high pressure again appears to be the result of flow stagnation where the environmental flow encounters the mesocyclone flow. Air parcels from both the low-level mesocyclone and the environmental flow are forced to descend in this stagnation zone leading to a warm arc of air on the west side of the storm's rear-flank (Fig. 13b). Variation in the strength of

the stagnation high pressure (speculated to be associated with storm and flow unsteadiness, including the non-steadiness of the updraft and the mesocyclone circulations) lead to pulses in the warm downdrafts (not shown).

Interestingly, Kumjian (2011) found anomalously large concentrations of small rain drops on the west side of the hook echo in his study. His favored hypothesis to explain the origin of the small drops was dynamically forced downdrafts from parcels that originated at low-levels (beneath the melting layer). These findings have recently been confirmed by French et al (2015), who found enhanced areas of small drops to the southwest of developing tornadoes observed by mobile Doppler radars. Moreover, French et al. (2015) showed that, in one case, an area of small drops descended faster than their fall speed would imply, implicating the downward advection of the drops by a downdraft. Given that thermodynamic observations show RFDs in tornadic supercells are relatively warm (Markowski et al. 2002; Grzych et al. 2007) and the fact that a buoyantly driven downdraft would likely derive its negative buoyancy from evaporation (resulting in paucity of small drops), French et al. (2015) speculate that this downdraft is dynamically forced. In addition, a recent modeling study by Kumjian et al. (2015) found an area of enhanced warm-rain mass mixing ratio collocated with a low-level downdraft in the hook echo of their simulated supercell. This is consistent with the observations discussed in Kumjian (2011) and French et al. (2015). While the single moment microphysics used in our study do not allow for detailed examination of the drop size distribution in our simulation, the location of the dynamically forced downdrafts in our study are similar to those proposed in Kumjian (2011) and French et al (2015) and seem to confirm the origin of the small drops found in these two studies.

d. Cold internal outflow surges

As discussed in the introduction, internal outflow surges have been found to have highly variable thermodynamic structures within a single storm (e.g., Lee et al 2012). Thus far, we have only discussed warm surges. However, our simulation also contains several cold surges especially during the mature and weakening phase of the first tornado. This tendency suggests that cold surges likely either have a negligible or possibly even negative impact on the simulated tornado. A similar relationship was noted in Finley et al. (2010) and Lee et al. (2012). In contrast, Marquis et al. (2012) found that despite negative buoyancy, in one case, a cold surge assisted in tornado maintenance. For completeness, we now investigate one of these cold surges. Examination of other cold surges in the simulation (not shown) indicate the general behavior and origin of the chosen cold internal outflow surge are fairly representative.

Fig. 14 presents a large cold surge that begins to emerge from the main downdraft around 2215. By 2219 (Fig. 14b), the surge has wrapped around tornado 1. Shortly thereafter, the surge begins to weaken and warm as more dynamically driven downdrafts re-develop around the tornado (see the developing warming in Fig. 14b near $x=28.0, y=13.5$). The development of the cold surge is slightly preceded by an intensification of tornado 1. This may suggest that the cold internal outflow surge accelerates horizontally towards the tornado owing to the pressure drop associated with the intensifying vortex near ground. Notably, large positive (to the left of the parcel velocity) crosswise horizontal vorticity is present at low levels in the cold internal outflow surge (Fig. 14c). This orientation of horizontal vorticity is nearly identical to that seen in the warm, tornado-triggering surge (SXH14) suggesting that frictional generation of horizontal vorticity is likely the dominant horizontal vorticity source term even in relatively cold outflow. This orientation of vorticity is opposite to that in the conceptual model of Marquis et al. (2012). But it is important to note that we are examining near-surface vorticity fields where frictional generation of vorticity is large (Fig. 14c) whereas Marquis et al. (2012) presented vortex lines intersecting vorticity

maxima at 400-m AGL (where frictional generation of vorticity is likely negligible) owing to radar sampling limitations.

Backward trajectories initiated within the cold internal outflow surge at 20-m AGL (Fig. 14b) originate from the south between 1-2.5 km AGL. As parcels enter the precipitation core of the storm they descend to the ground and then accelerate to the southeast toward the tornado. Forcing terms along a representative backward trajectory (Fig. 15a) confirm that the parcel descent is forced buoyantly by both evaporative cooling and effective water loading. Moreover, crosswise vorticity budgets calculated along this trajectory (Fig. 15b; see SXH14 for more details on vorticity budget calculations) show that baroclinic generation of crosswise vorticity is initially dominant while the parcel is far above the ground but the frictional term becomes dominant as the parcel approaches the ground. This analysis confirms that frictionally generated vorticity is indeed responsible for the large near-surface positive crosswise vorticity within the cold surge. It is worth mentioning that the best way to handle the parameterization of surface drag in strongly sheared, unsteady flow on anisotropic grids is an area of active research. As such, the model may not be accurately representing the surface drag. However, it stands to reason that the sign of frictionally generated vorticity should be correct even if the magnitude may be incorrect.

5. Summary and discussion

This paper has examined the forcing for internal outflow surges within a tornado-resolving high-resolution simulation of the 8 May 2003 Oklahoma City tornadic supercell. This simulation forecasted the development of two tornadoes that took a similar track as the observed long-track tornado. Internal outflow surges have been noted to be important in tornadogenesis (e.g., Mashiko et al. 2009; Kosiba et al. 2013) and maintenance (e.g., Marquis et al. 2012). In their examination of this simulation, SXH14 found many internal outflow surges with one, in particular, that appeared to act as a trigger for tornadogenesis within the first simulated tornado. However, SXH14 did not examine the cause of this or other simulated internal outflow surges.

Through trajectory analysis and diagnosis of the buoyant and dynamic components of the vertical momentum forcing along the trajectories, this study determined that the warm internal outflow surges (including the tornado-triggering one) in this simulation were predominantly dynamically forced by relatively-high stagnation pressure between the environmental flow and the mesocyclone at the mid-lower levels. In the case of the tornado-triggering surge, the instigating area of relatively-high perturbation pressure was small in areal extent and short-lived, explaining in turn the small-scale and transient nature of this surge. A more persistent area of perturbation high pressure on the southwest side of the mesocyclone led to an arc of warm downdrafts on the west side of the simulated tornado. These warm downdrafts were in a similar storm- and tornado-relative position to areas of small rain drops found in the observational studies of Kumjian (2011) and French et al. (2015), which suggested that the parcels carrying these drops dynamically descend from the mid-lower levels below the freezing level.

A cold internal outflow surge was also examined in this study. Not surprisingly, this surge originated via effective buoyancy forcing in the storm's main downdraft. Cold surges occurred mainly during the mature and weakening stages of the tornado suggesting they may have a negative impact on the tornado due to the negative effective buoyancy they possess. Their occurrence may also be modulated by the tornado itself as the cold surge examined herein was slightly preceded by tornado intensification.

As with most single case studies of high-resolution numerical simulations, the present study comes with the caveat that results may vary wildly on a case-to-case basis. As such, it is

important not to focus on the details of the analysis presented herein. More important is the physical processes described whereby the internal outflow surges develop. To our knowledge, this study is the first to attribute the development of internal outflow surges to the stagnation pressure as described herein. Skinner et al. (2014) also found that internal outflow surges in their study were forced by a dynamic vertical pressure gradient. However, in their case, they suggest that the downdrafts responsible for the internal outflow surges are similar to occlusion downdrafts. Namely, the downdrafts are forced by stronger rotation and the associated pressure drop at low-levels. Reconciling these differences will require additional observational and numerical studies.

Unfortunately, the small spatio-temporal scale of the region of perturbation high pressure found to be responsible for the tornado-triggering internal outflow surge is not particularly promising for forecasting tornadogenesis. However, it may be possible to come up with a probabilistic criterion that an internal outflow surge, given a supercell and its environmental characteristics, is more (or less) likely to trigger a tornado at some point in the near future. Future work will examine more cases to determine the generality of the results found in this study. In addition, it may be possible with more studies to develop or determine a more useful metric that could be used in a more operational setting to forecast the development of internal outflow surges.

Acknowledgement: This work was primarily supported by NSF grant AGS-0802888. The second author was also supported by NSF grants AGS-1046171 and AGS-1261776. The third author was also supported by an NSF Post-doctoral Fellowship. Numerical simulations were performed at the University of Oklahoma Supercomputing Center for Education and Research (OSKER) and at the Pittsburgh Supercomputing Center. Comments from three anonymous reviewers were instrumental in clarifying and enhancing the content of this manuscript. The first author thanks Drs. Pat Skinner, Matthew Kumjian, and Mike French for helpful discussions.

References

- Adams, J., 1989: MUDPACK: Multigrid portable FORTRAN software for the efficient solution of linear elliptic partial differential equations. *Appl. Math. Comput.*, **34**, 113-146.
- Adlerman, E. J., 2003: Numerical simulations of cyclic storm behaviors: Mesocyclogenesis and tornadogenesis, Ph.D. Dissertation, School of Meteorology, University of Oklahoma, 219 pp.
- Beck, J. and C. Weiss, 2013: An Assessment of Low-Level Baroclinity and Vorticity within a Simulated Supercell. *Mon Weather Rev*, **141**, 649-669.
- Beck, J. R., J. L. Schroeder, and J. M. Wurman, 2006: High-resolution dual-Doppler analyses of the 29 May 2001 Kress, Texas, cyclic supercell. *Mon Weather Rev*, **134**, 3125-3148.
- Biggerstaff, M. I., L. J. Wicker, J. Guynes, J. Doggett, C. Ziegler, J. M. Straka, E. N. Rasmussen, A. D. IV, L. D. Carey, and J. L. Schroeder, 2005: The shared mobile atmospheric research and teaching (SMART) radar: A collaboration to enhance research and teaching. *Bull. Amer. Meteor. Soc.*, **86**, 1263-1274.
- Bluestein, H. B., M. M. French, I. PopStefanija, R. T. Bluth, and J. B. Knorr, 2010: A Mobile, Phased-Array Doppler Radar for the Study of Severe Convective Storms the Mwr-05xp. *B Am Meteorol Soc*, **91**, 579-+.
- Dahl, J. M. L., M. D. Parker, and L. Wicker, 2012: Uncertainties in trajectory calculations within near-surface mesocyclones of simulated supercells. *Mon. Wea. Rev.*, **140**, 2959-2966.
- Davies-Jones, R., 2003: An Expression for Effective Buoyancy in Surroundings with Horizontal Density Gradients. *J. Atmos. Sci.*, **60**, 2922-2925.

- Dawson, D. T., II, M. Xue, A. Shapiro, J. A. Milbrandt, and A. D. Schenkman, 2015: Sensitivity of real-data simulations of the 3 May 1999 Oklahoma City tornadic supercell and associated tornadoes to multi-moment microphysics. Part II: analysis of buoyancy and dynamic pressure forces in simulated tornado-like vortices. *J. Atmos. Sci.*, **Conditionally Accepted**.
- Doswell, C. A. and P. M. Markowski, 2004: Is buoyancy a relative quantity? *Mon Weather Rev*, **132**, 853-863.
- Emanuel, K. A., 1994: *Atmospheric Convection*. Oxford Univ. Press, 580 pp.
- Finley, C. A. and B. D. Lee, 2008: Mobile mesonet observations of an intense RFD and multiple RFD gust fronts in the May 23 Quinter, Kansas tornadic supercell during TWISTEX 2008. *24th Conf. on Severe Local Storms*, Amer. Meteor. Soc.
- Finley, C. A., B. D. Lee, C. D. Karstens, M. Grzych, and T. M. Samaras, 2010: Mobile mesonet observations of the rear-flank downdraft evolution associated with a violent tornado near Bowdle, SD on 22 May 2010. *25th Conf. on Severe Local Storms*, Amer. Meteor. Soc.
- French, M. M., D. W. Burgess, E. R. Mansell, and L. J. Wicker, 2015: Bulk hook echo raindrop sizes retrieved using mobile, polarimetric Doppler radar observations. *J. Appl. Meteor. Climatol.*, **54**, 423-450.
- Grzych, M., B. D. Lee, and C. A. Finley, 2007: Thermodynamic analysis of supercell rear-flank downdrafts from project ANSWERS. *Mon. Wea. Rev.*, **135**, 240-246.
- Hirth, B. D., J. L. Schroeder, and C. Weiss, 2008: Surface analysis of the rear-flank downdraft outflow in two tornadic supercells. *Mon. Wea. Rev.*, **136**, 2344-2363.
- Hu, M. and M. Xue, 2007: Impact of configurations of rapid intermittent assimilation of WSR-88D radar data for the 8 May 2003 Oklahoma City tornadic thunderstorm case. *Mon. Wea. Rev.*, **135**, 507-525.
- Jeevanjee, N. and D. M. Romps, 2015: Effective buoyancy, inertial pressure, and the mechanical generation of boundary layer mass flux by cold pools. *J. Atmos. Sci.*, **72**, 3199-3213.
- Kosiba, K., J. Wurman, Y. Richardson, P. Markowski, P. Robinson, and J. Marquis, 2013: Genesis of the Goshen County, Wyoming, Tornado on 5 June 2009 during VORTEX2. *Mon Weather Rev*, **141**, 1157-1181.
- Kumjian, M., 2011: Precipitation properties of supercell hook echoes. *Electron. J. Severe Storms Meteor*, **6**, 1-21.
- Kumjian, M. R., Z. J. Lebo, and H. C. Morrison, 2015: On the mechanisms of rain formation in an idealized supercell storm. *Mon. Wea. Rev.*, **143**, 2754-2773.
- Lee, B. D., C. A. Finley, and T. M. Samaras, 2011: Surface analysis near and within the Tipton, Kansas, Tornado on 29 May 2008. *Mon. Wea. Rev.*, **139**.
- Lee, B. D., C. A. Finley, and C. D. Karstens, 2012: The Bowdle, South Dakota, Cyclic Tornadic Supercell of 22 May 2010: Surface Analysis of Rear-Flank Downdraft Evolution and Multiple Internal Surges. *Mon Weather Rev*, **140**, 3419-3441.
- Lin, Y.-L., R. D. Farley, and H. D. Orville, 1983: Bulk parameterization of the snow field in a cloud model. *J. Climat. Appl. Meteor.*, **22**, 1065-1092.
- Markowski, P., E. Rasmussen, J. Straka, R. Davies-Jones, Y. Richardson, and R. J. Trapp, 2008: Vortex lines within low-level mesocyclones obtained from pseudo-dual-doppler radar observations. *Mon Weather Rev*, **136**, 3513-3535.
- Markowski, P. M., J. M. Straka, and E. N. Rasmussen, 2002: Direct surface thermodynamic observations within the rear-flank downdrafts of nontornadic and tornadic supercells. *Mon. Wea. Rev.*, **130**, 1692-1721.

- Marquis, J., Y. Richardson, J. Wurman, and P. Markowski, 2008: Single- and Dual-Doppler Analysis of a Tornadic Vortex and Surrounding Storm-Scale Flow in the Crowell, Texas, Supercell of 30 April 2000. *Mon Weather Rev*, **136**, 5017-5043.
- Marquis, J., Y. Richardson, P. Markowski, D. Dowell, and J. Wurman, 2012: Tornado Maintenance Investigated with High-Resolution Dual-Doppler and EnKF Analysis. *Mon. Wea. Rev.*, **140**, 3-27.
- Mashiko, W., H. Niino, and T. Kato, 2009: Numerical Simulation of Tornadogenesis in an Outer-Rainband Minisupercell of Typhoon Shanshan on 17 September 2006. *Mon Weather Rev*, **137**, 4238-4260.
- Pazmany, A. L., J. B. Mead, H. B. Bluestein, J. C. Snyder, and J. B. Houser, 2013: A Mobile Rapid-Scanning X-band Polarimetric (RaXPoL) Doppler Radar System. *J Atmos Ocean Tech*, **30**, 1398-1413.
- Romine, G. S., D. W. Burgess, and R. B. Wilhelmson, 2008: A Dual-Polarization-Radar-Based Assessment of the 8 May 2003 Oklahoma City Area Tornadic Supercell. *Mon. Wea. Rev.*, **136**, 2849-2870.
- Schenkman, A., M. Xue, and M. Hu, 2014: Tornadogenesis within numerically simulated 8 May 2003 Oklahoma City tornadic supercell storm. *J. Atmos. Sci.*, **71**, 130-154.
- Skinner, P. S., C. C. Weiss, J. L. Schroeder, L. J. Wicker, and M. I. Biggerstaff, 2011: Observations of the Surface Boundary Structure within the 23 May 2007 Perryton, Texas, Supercell. *Mon Weather Rev*, **139**, 3730-3749.
- Skinner, P. S., C. C. Weiss, M. M. French, H. B. Bluestein, P. M. Markowski, and Y. P. Richardson, 2014: VORTEX2 observations of a low-level mesocyclone with multiple internal rear-flank downdraft momentum surges in the 18 May 2010 Dumas, Texas, supercell. *Mon Weather Rev*, **142**, 2935-2960.
- Straka, J., E. Rasmussen, R. Davies-Jones, and P. Markowski, 2007: An observational and idealized numerical examination of low-level counter-rotating vortices toward the rear flank of supercells. *Electron. J. Severe Storms Meteor*, **2**, 1-22.
- Tao, W.-K. and J. Simpson, 1993: The Goddard Cumulus Ensemble Model. Part I: Model description. *Terrestrial, Atmospheric and Oceanic Sciences*, **4**, 35-72.
- Wurman, J., J. Straka, E. Rasmussen, M. Randall, and A. Zahrai, 1997: Design and deployment from a portable, pencil-beam, pulsed, 3-cm Doppler radar. *J. Atmos. Ocean Tech.*, **14**, 1502-1512.
- Wurman, J., Y. Richardson, C. Alexander, S. Weygandt, and P. F. Zhang, 2007a: Dual-Doppler and single-Doppler analysis of a tornadic storm undergoing mergers and repeated tornadogenesis. *Mon Weather Rev*, **135**, 736-758.
- Wurman, J., Y. Richardson, C. Alexander, S. Weygandt, and P. F. Zhang, 2007b: Dual-Doppler analysis of winds and vorticity budget terms near a tornado. *Mon Weather Rev*, **135**, 2392-2405.
- Wurman, J., K. Kosiba, P. Markowski, Y. Richardson, D. Dowell, and P. Robinson, 2010: Finescale Single- and Dual-Doppler Analysis of Tornado Intensification, Maintenance, and Dissipation in the Orleans, Nebraska, Supercell. *Mon Weather Rev*, **138**, 4439-4455.
- Xue, M., M. Hu, and A. Schenkman, 2014: Numerical prediction of 8 May 2003 Oklahoma City tornadic supercell and embedded tornado using ARPS with the assimilation of WSR-88D radar data. *Wea. Forecasting*, **29**, 39-62.

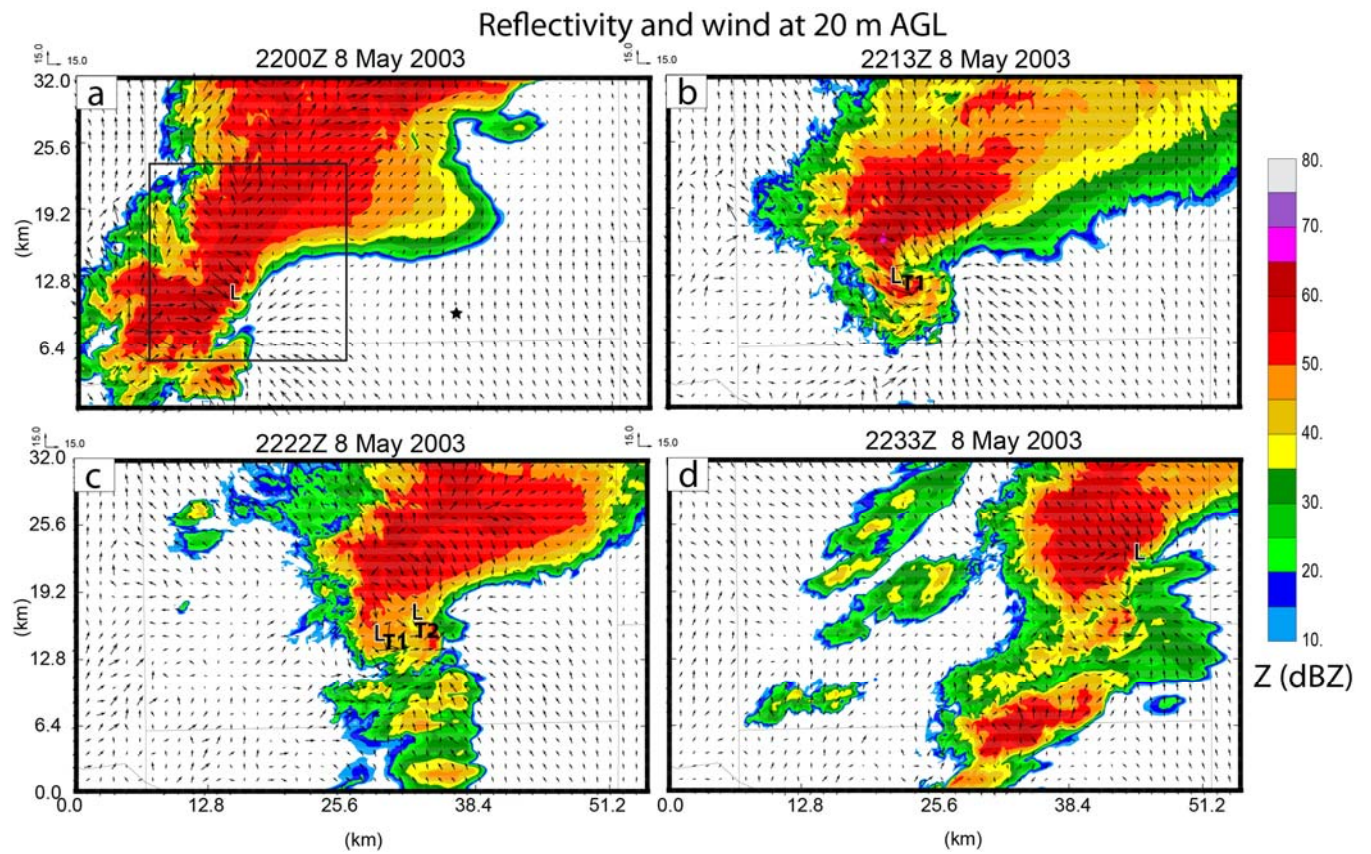


Fig. 1 Simulated reflectivity factor (dBZ) and horizontal ground-relative wind vectors (m s^{-1}) at 20 m AGL at (a) 2200 UTC, (b) 2213 UTC, (c) 2222 UTC, and (d) 2233 UTC on 8 May 2003. The black box in (a) marks the plotted area in Fig. 2. The letters 'L', 'T1', and 'T2' mark the location of the low-level mesocyclone(s) and tornadoes 1 and 2, respectively.

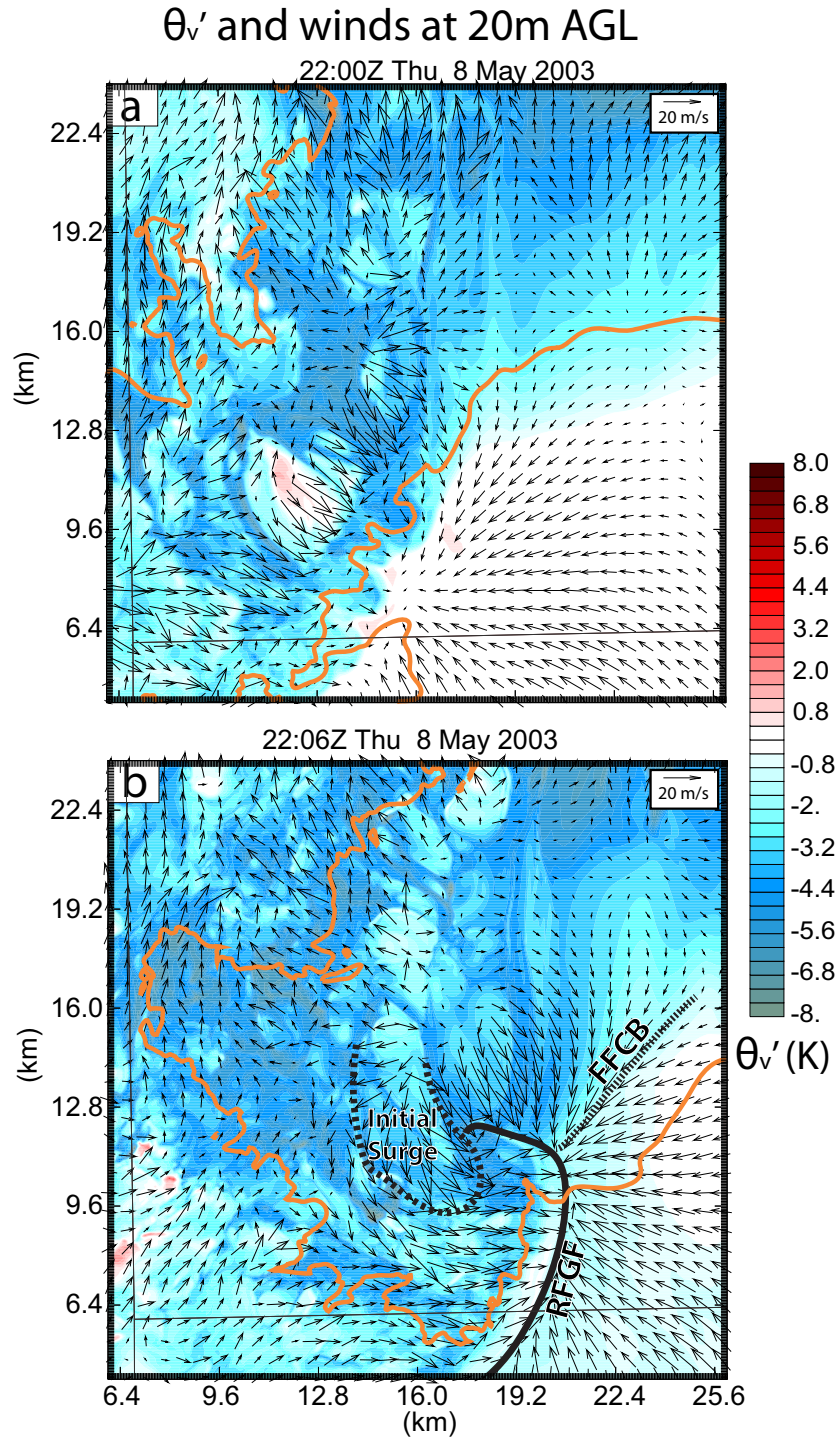


Fig. 2. Perturbation virtual potential temperature (K) and ground-relative wind vectors (m/s) at 20 m AGL at (a) 2200 UTC and (b) 2206 UTC. The thick orange line marks the location of the 40 dBZ contour. The black solid, short dashed and long-dashed lines mark the location of the RFGF, FFCB, and an internal outflow surge, respectively.

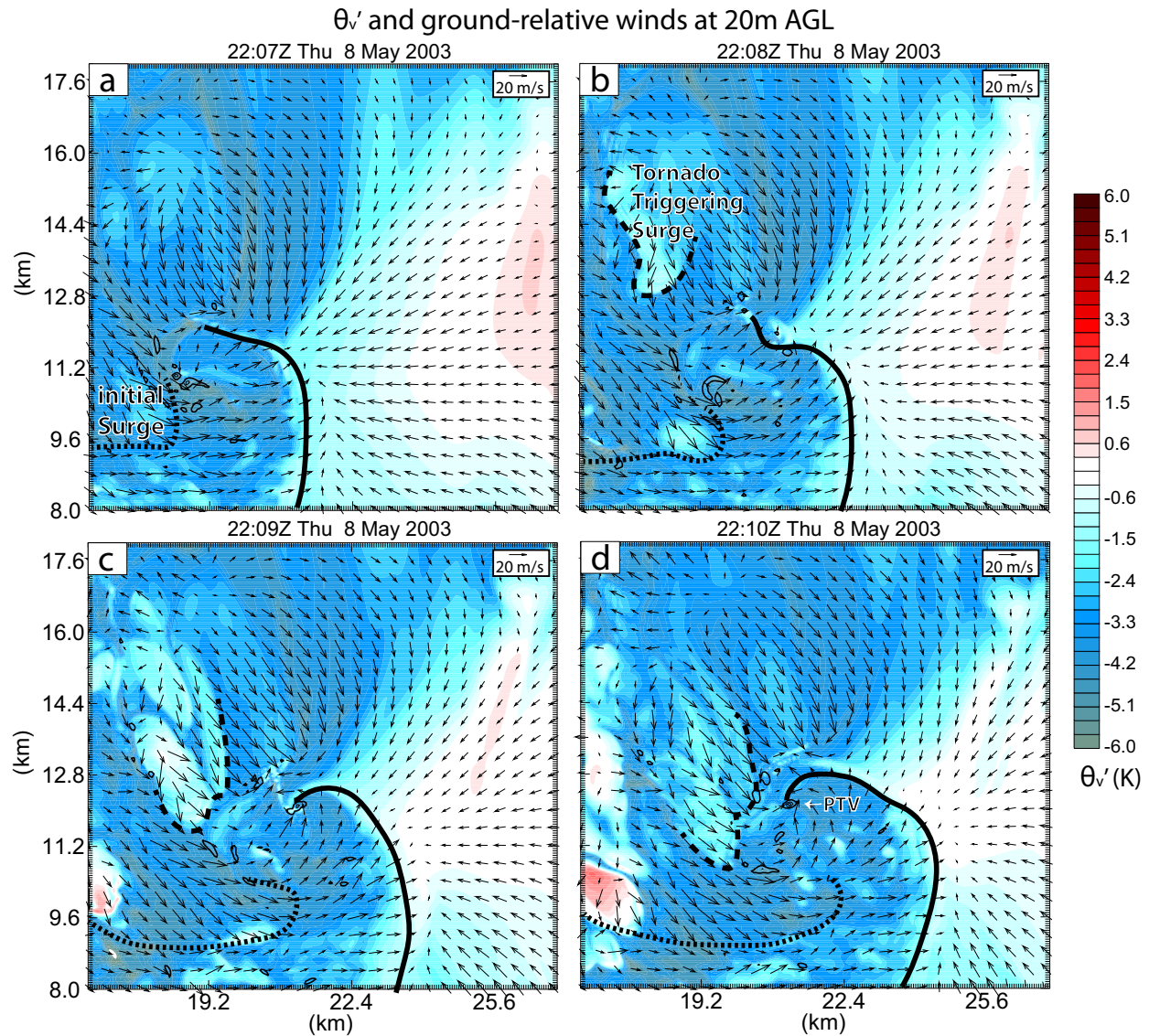


Fig. 3 Perturbation virtual potential temperature (shaded, K), ground-relative wind vectors (m/s), and vertical vorticity (0.3 s^{-1} increment contours starting at 0.1 s^{-1}) at 20 m AGL at (a) 2207 UTC, (b) 2208 UTC, (c) 2209 UTC, and (d) 2210 UTC. The solid, long-dashed, and short-dashed lines denote the subjectively analyzed location of the RFGF, initial internal outflow surge, and tornado-triggering internal outflow surge, respectively. ‘PTV’ marks the location of the pre-tornadic vortex. Note the color scale limits have been reduced from Fig. 2 in order to better show the internal outflow surges.

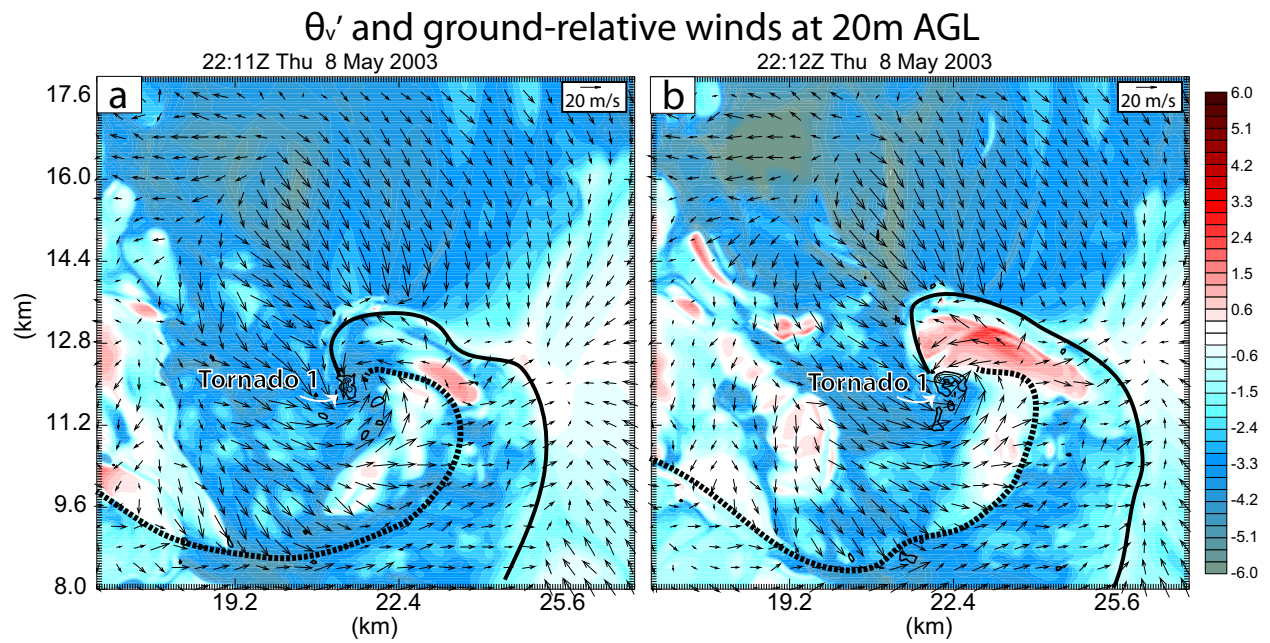


Fig. 4. As Fig. 3 but at (a) 2211 UTC and (b) 2212 UTC. The initial and tornado-triggering internal outflow surge have merged and are marked by the short-dashed line.

θ'_v and winds at 20m AGL

22:22Z Thu 8 May 2003

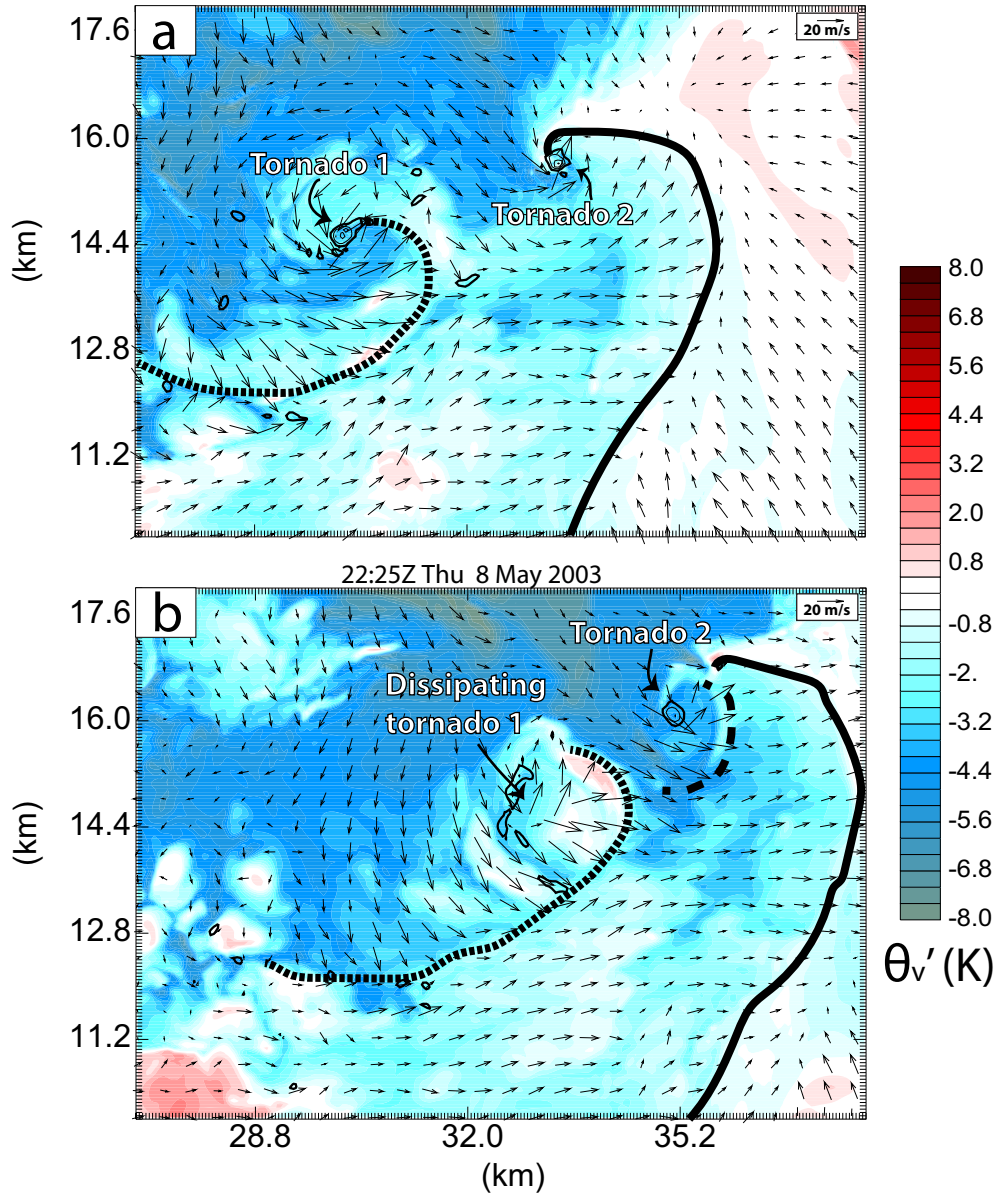


Fig. 5. As Fig. 3 but at (a) 2222 UTC and (b) 2225 UTC. The short dashed line marks an internal outflow surge associated with tornado 1. In (b), the long-dashed line marks the leading edge of a new internal outflow surge associated with tornado 2.

θ_v' and winds at 20m AGL

22:10Z Thu 8 May 2003

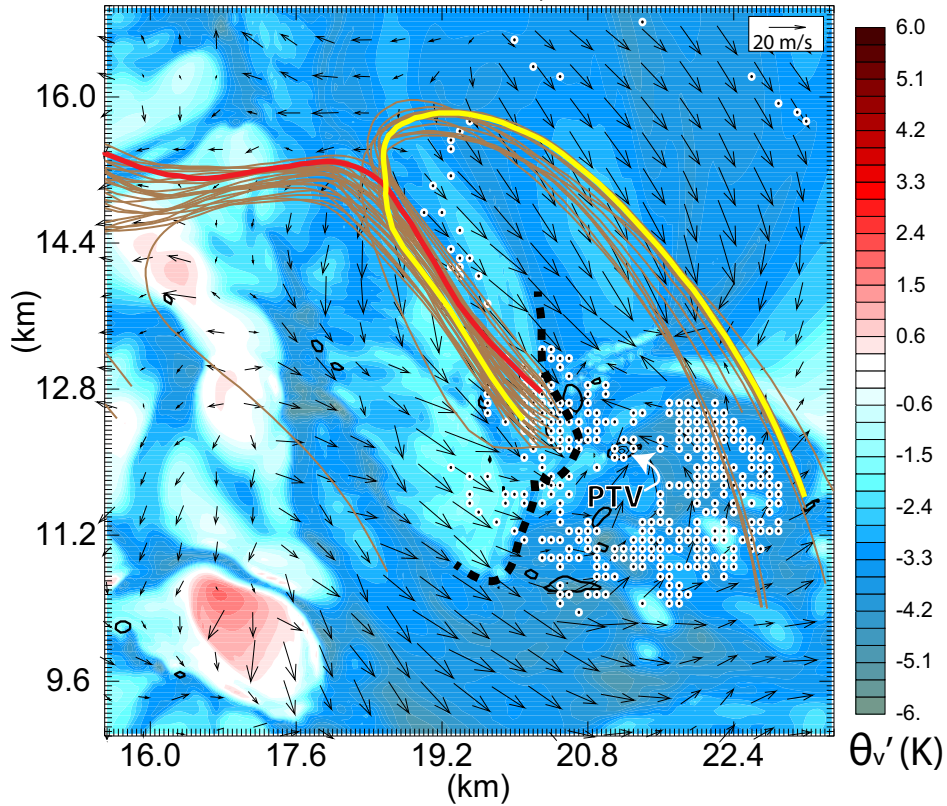


Fig. 6. As Fig. 3 but at 2210 UTC. White circles mark the locations of forward trajectories that enter the tornado in the subsequent five minutes. Brown lines mark backward trajectories that terminate in the internal outflow surge and subsequently enter the simulated tornado. The dashed black line marks the leading edge of the tornado-triggering internal outflow surge. The RFGF is unmarked for better visibility of the trajectories and parcel locations. Vertical forcing terms along the red and yellow trajectory are presented in Fig. 7a and Fig. 7b, respectively.

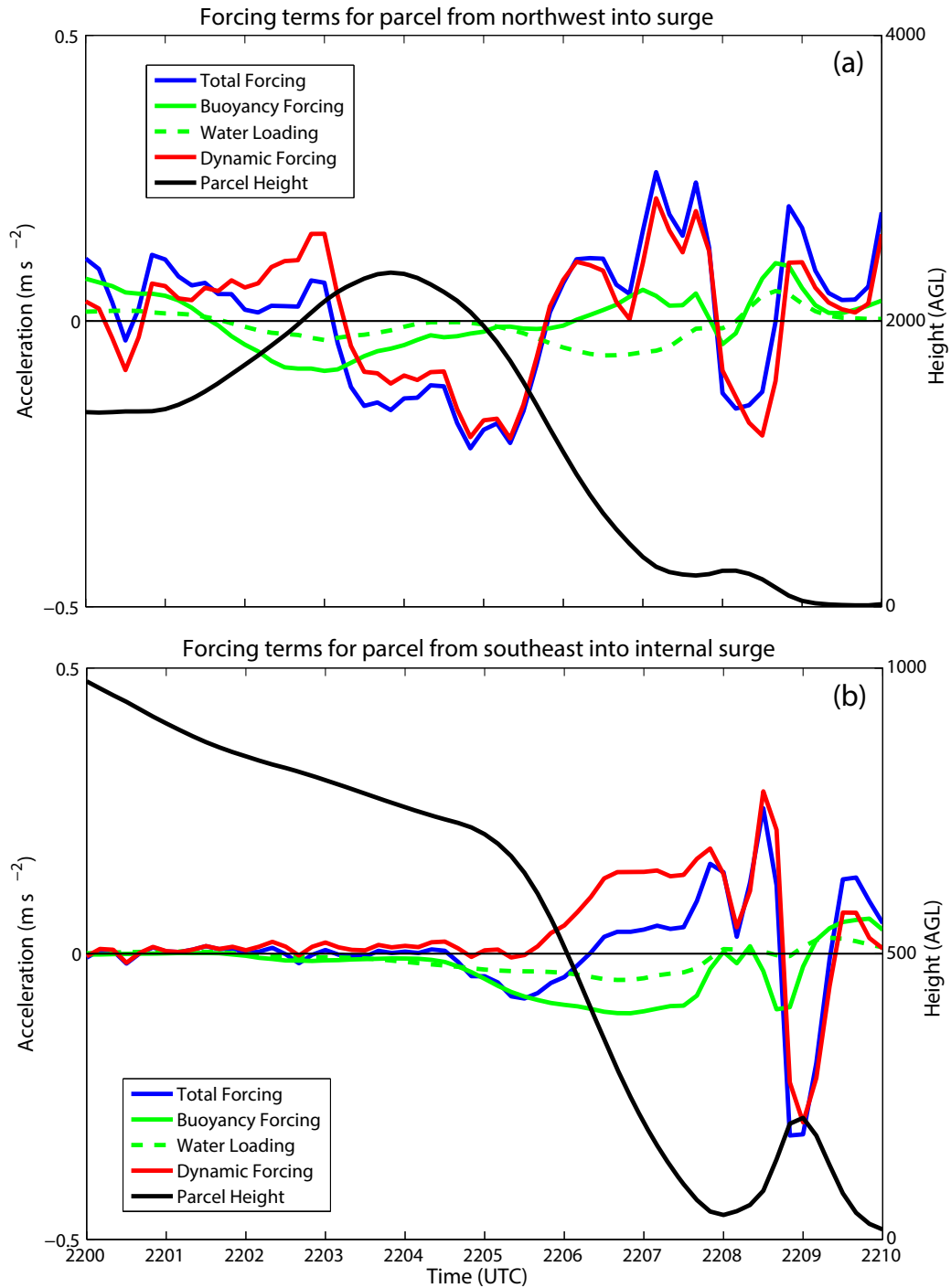


Fig. 7. Forcing terms along (a) the red and (b) the yellow backward trajectory in Fig. 6 within the tornado-triggering internal outflow surge. The blue line is the sum of the effective buoyancy (green line) and dynamic forcing (red line). The dashed green line is the effective water loading term. The black line represents the parcel height AGL corresponding to the axis label on the right.

θ'_v and ground-relative winds at 20m AGL

22:09Z Thu 8 May 2003

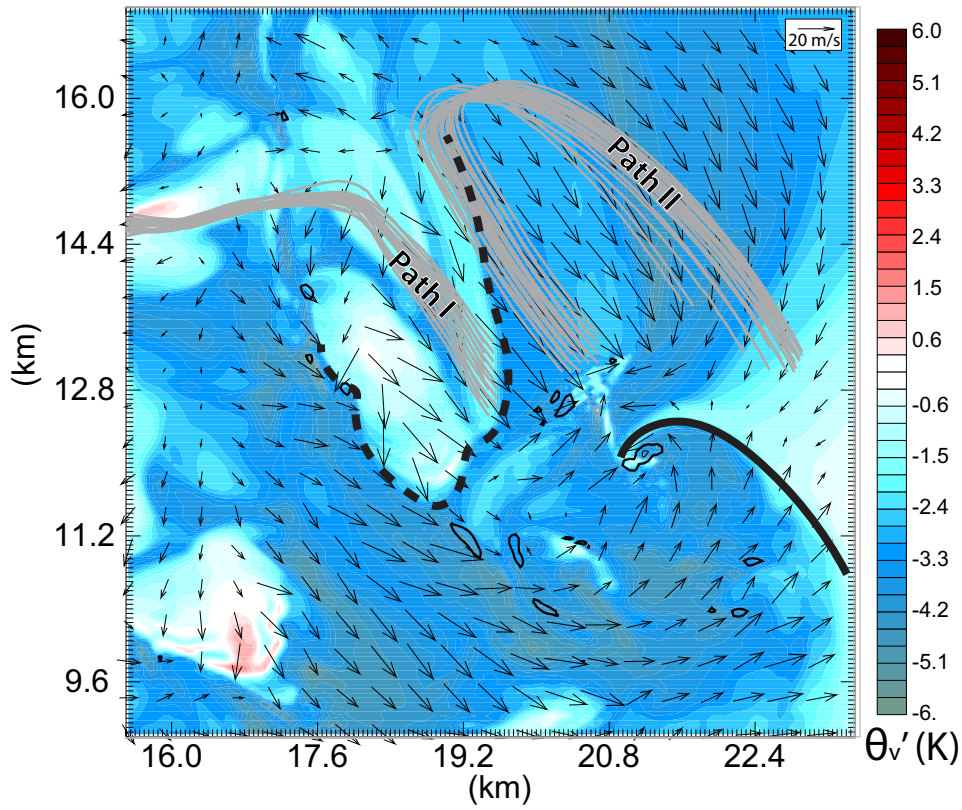


Fig. 8. As Fig. 6 but at 2209 UTC. Gray lines are backward parcel trajectories.

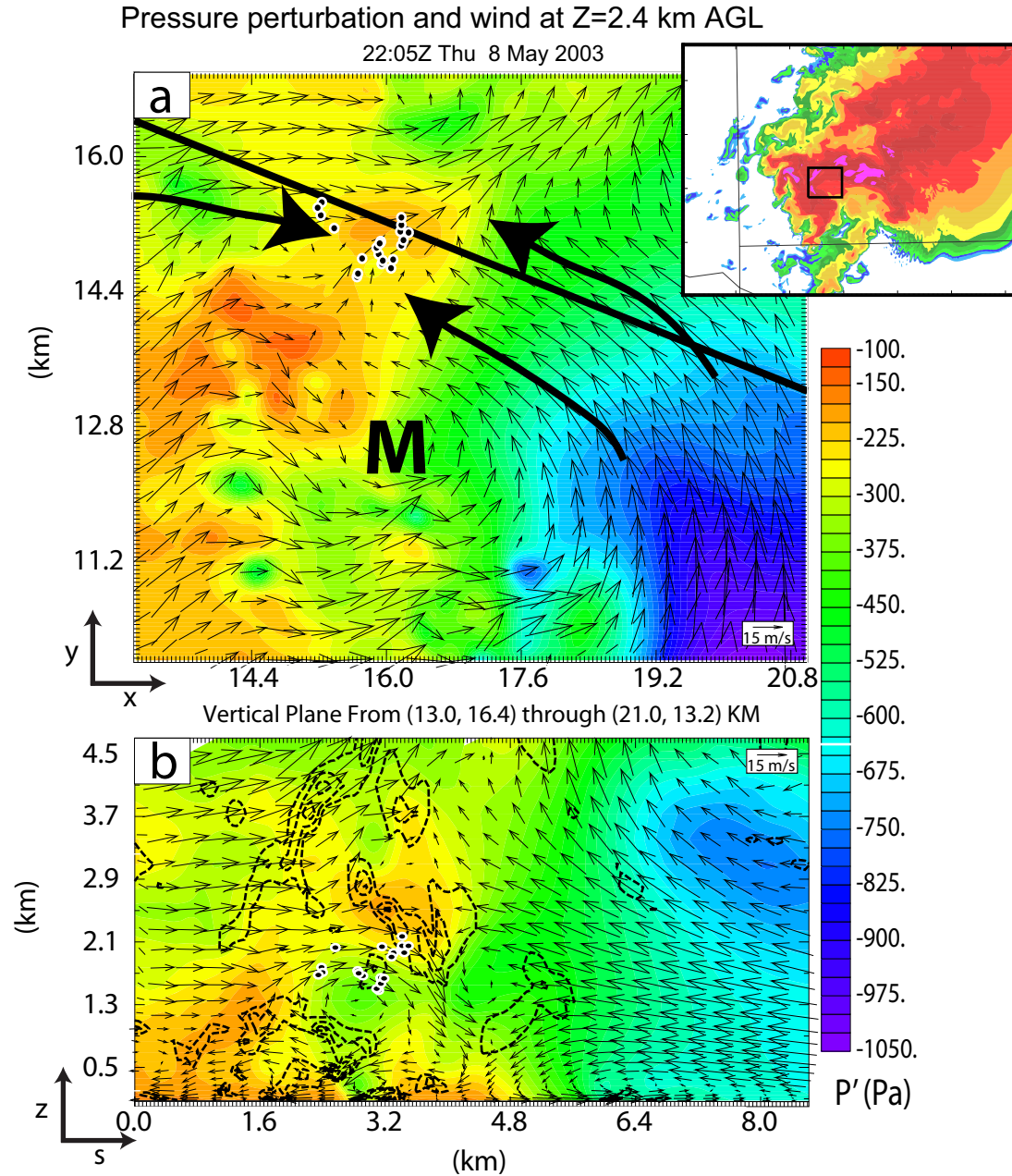


Fig. 9. Pressure perturbation (shaded, Pa) and ground-relative wind vectors (m/s) at 2205 UTC for an (a) x-y plane at 2.4 km AGL and (b) vertical cross-section along the heavy black line (z-s plane, where 's' is along the heavy black line in (a) towards the southeast) in (a). The black outlined box on the reflectivity plot in the upper right corner marks the plotted area in (a). Reflectivity contours are as Fig. 1. White outlined black dots mark the location (projected into the plotted plane) of the backward trajectories in group I from Fig. 6. The 'M' in (a) marks the center of the low-level mesocyclone. The large black arrows in (a) illustrate the convergence between the environmental flow and the southeasterly low-level mesocyclone flow. Horizontal divergence is plotted (-0.01 s^{-1} increment dashed line contours starting at -0.01 s^{-1}) in (b).

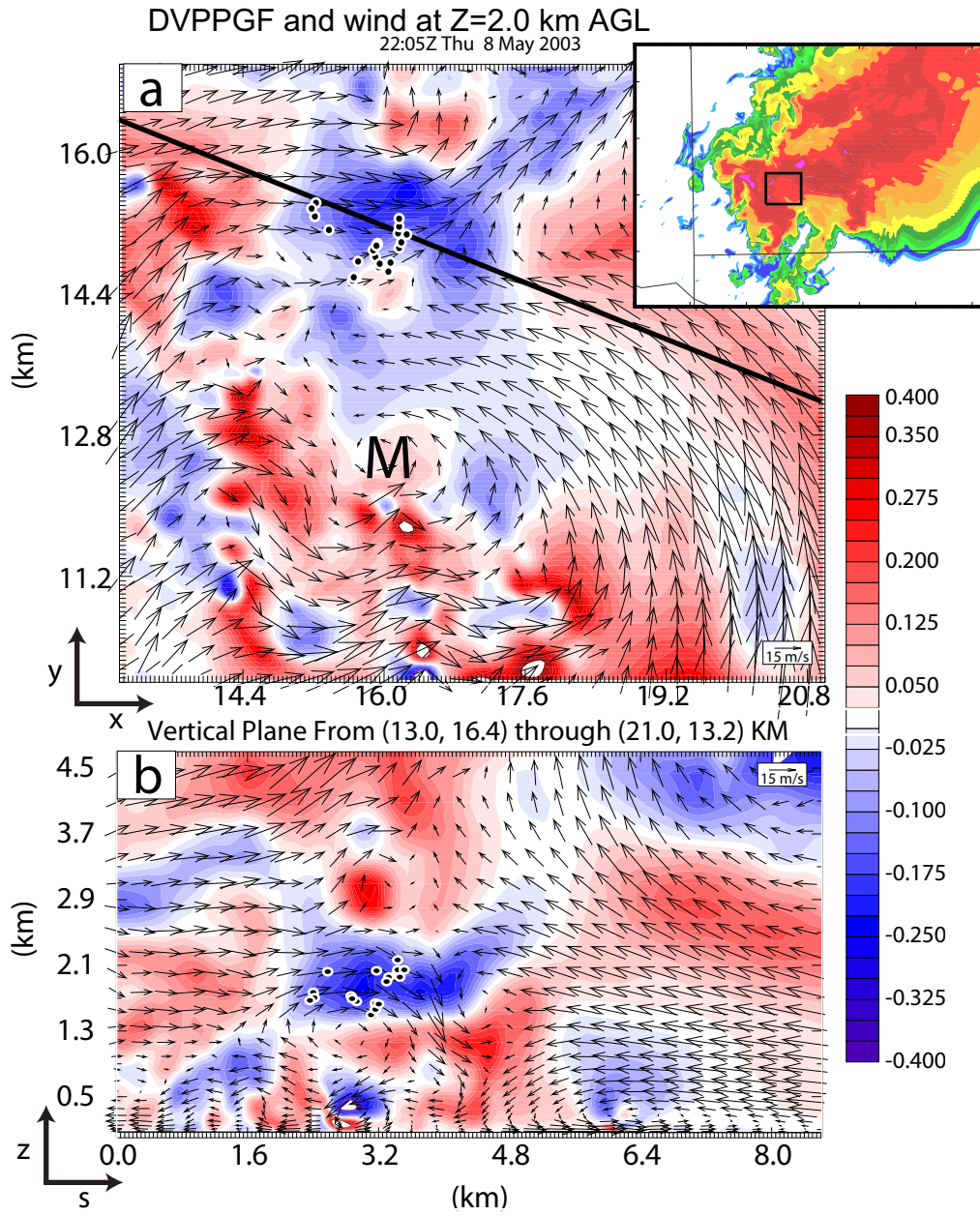


Fig. 10. As Fig. 9 but for DVPPGF (shaded, m s^{-2}) at 2 km AGL.

θ'_v and winds at 20m AGL

22:13Z Thu 8 May 2003

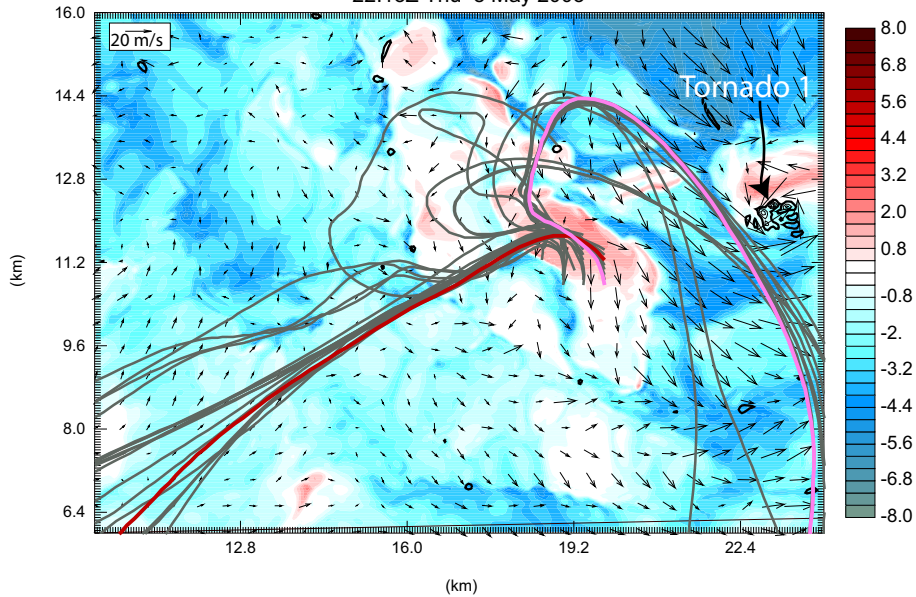


Fig. 11. Perturbation virtual potential temperature (shaded, K) and ground-relative wind vectors (m s^{-1}) and vertical vorticity (0.3 s^{-1} increment contours starting at 0.1 s^{-1}) at 2213 UTC. Solid gray lines mark backward trajectories that terminate in a warm pocket of air. The red and purple lines mark the chosen representative trajectories.

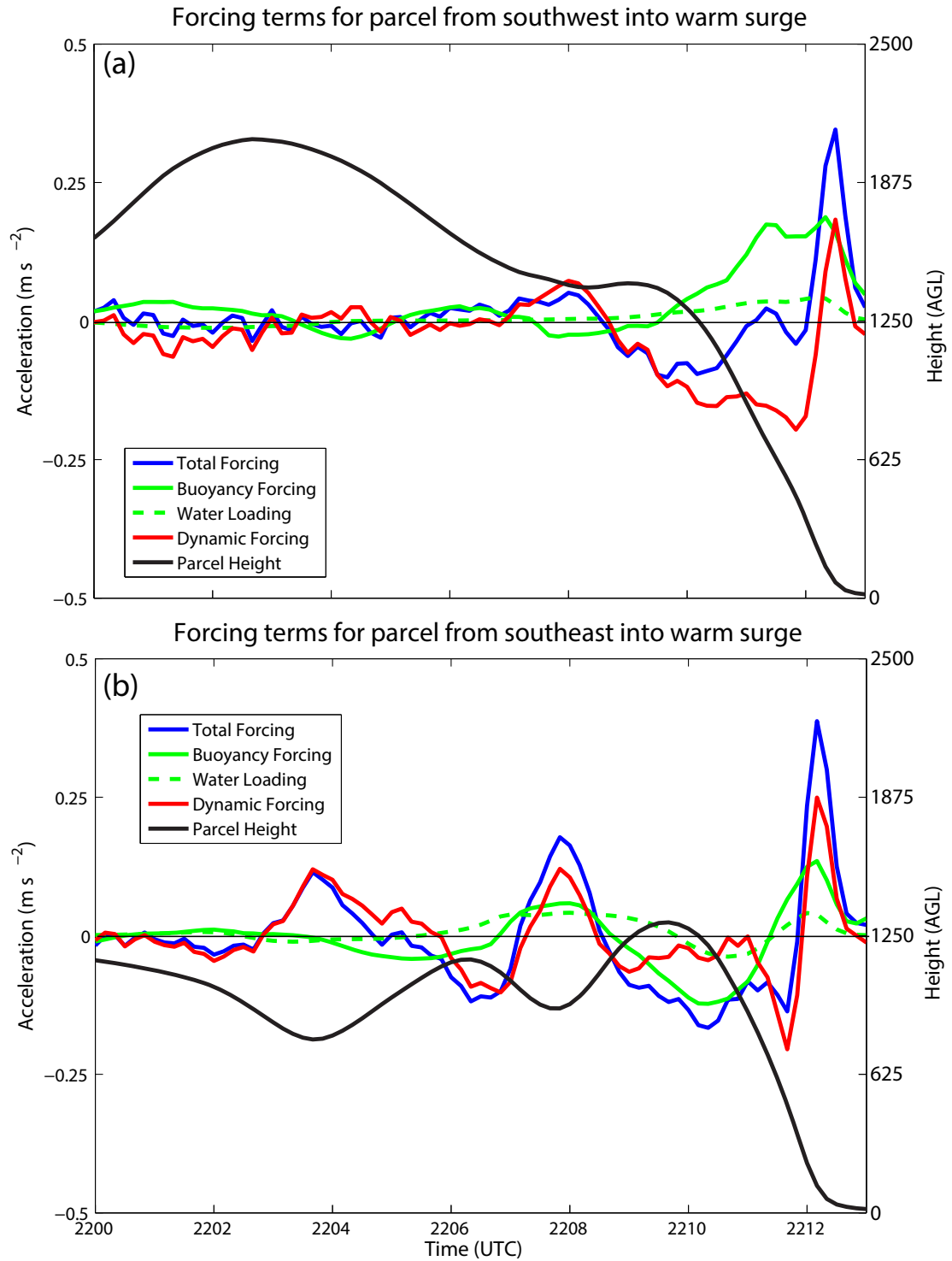


Fig. 12. Forcing terms calculated along the two representative trajectories in Fig. 11. The blue line is the sum of then effective buoyancy (green line) and dynamic forcing (red line). The black line is the trajectory height AGL. The dashed green line is the effective water loading term.

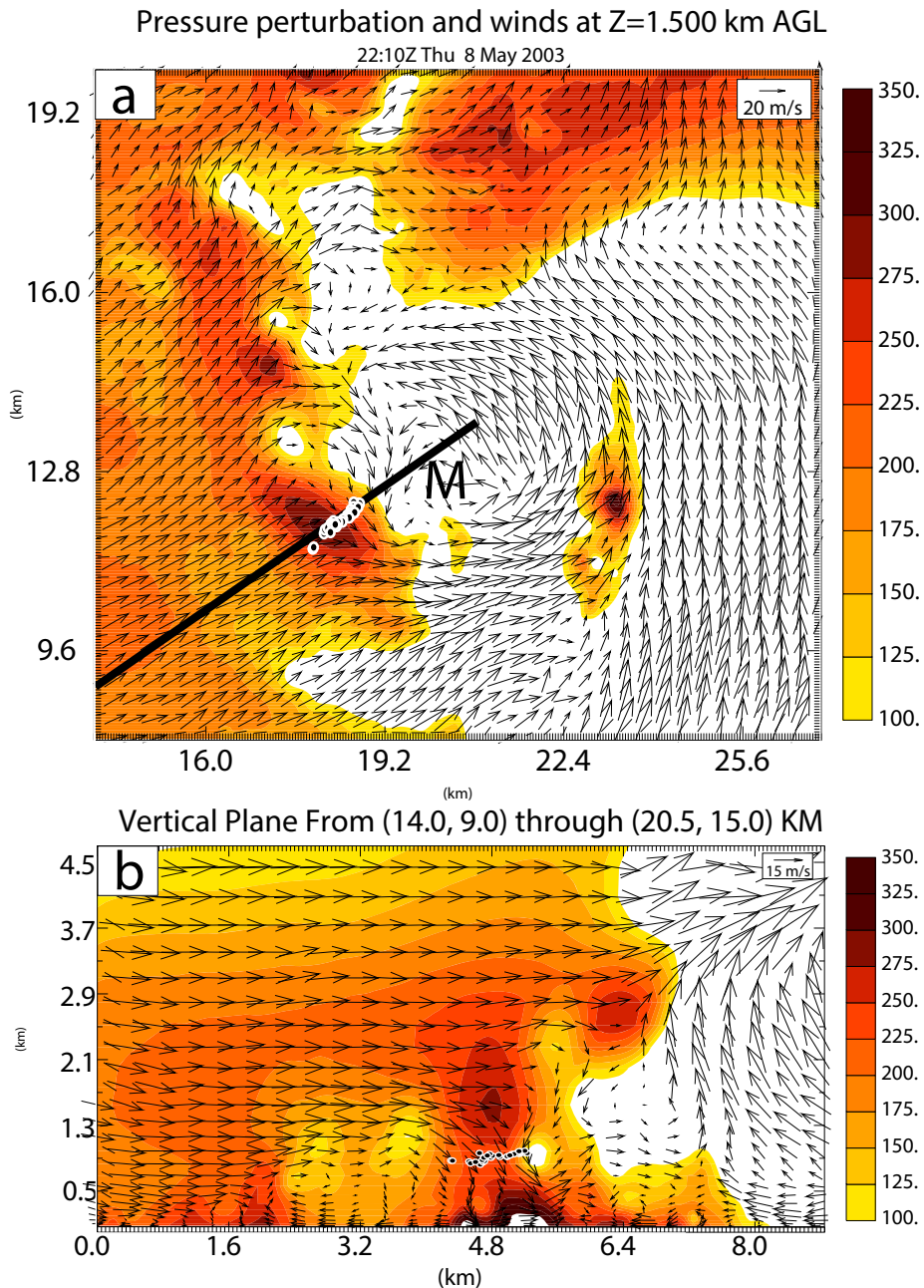


Fig. 13. Pressure perturbation (shaded > 100 Pa) at 2210 UTC for an (a) X-Y plane at 1.5 km AGL and (b) a vertical cross-section along the dark black line in (a). The 'M' marks the approximate center of the mesocyclone. White outlined black dots mark the location of the parcels in Fig. 11 projected into the plotted planes.

θ'_v and ground-rel winds at 20 m AGL

22:15Z Thu 8 May 2003

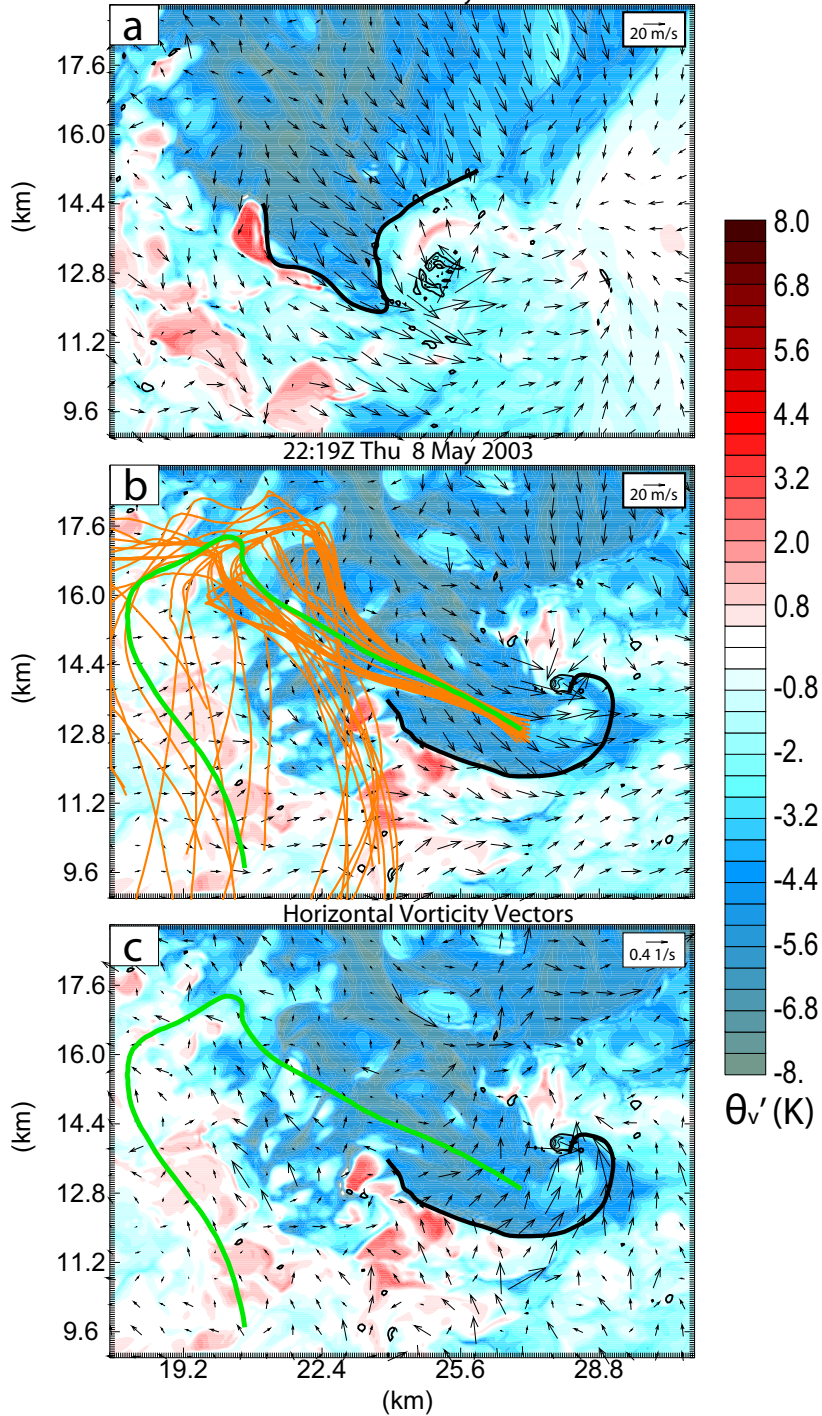


Fig. 14. As Fig. 11 but at (a) 2215 and (b) 2219 UTC. In (c), 2219 UTC is plotted but with horizontal vorticity vectors instead of wind vectors. The thick black line marks the leading edge of the cold internal outflow surge. Orange lines mark parcel trajectories into the cold surge. The green line in (b) and (c) is representative trajectory over which forcing and vorticity budgets are calculated and presented in Fig. 15.

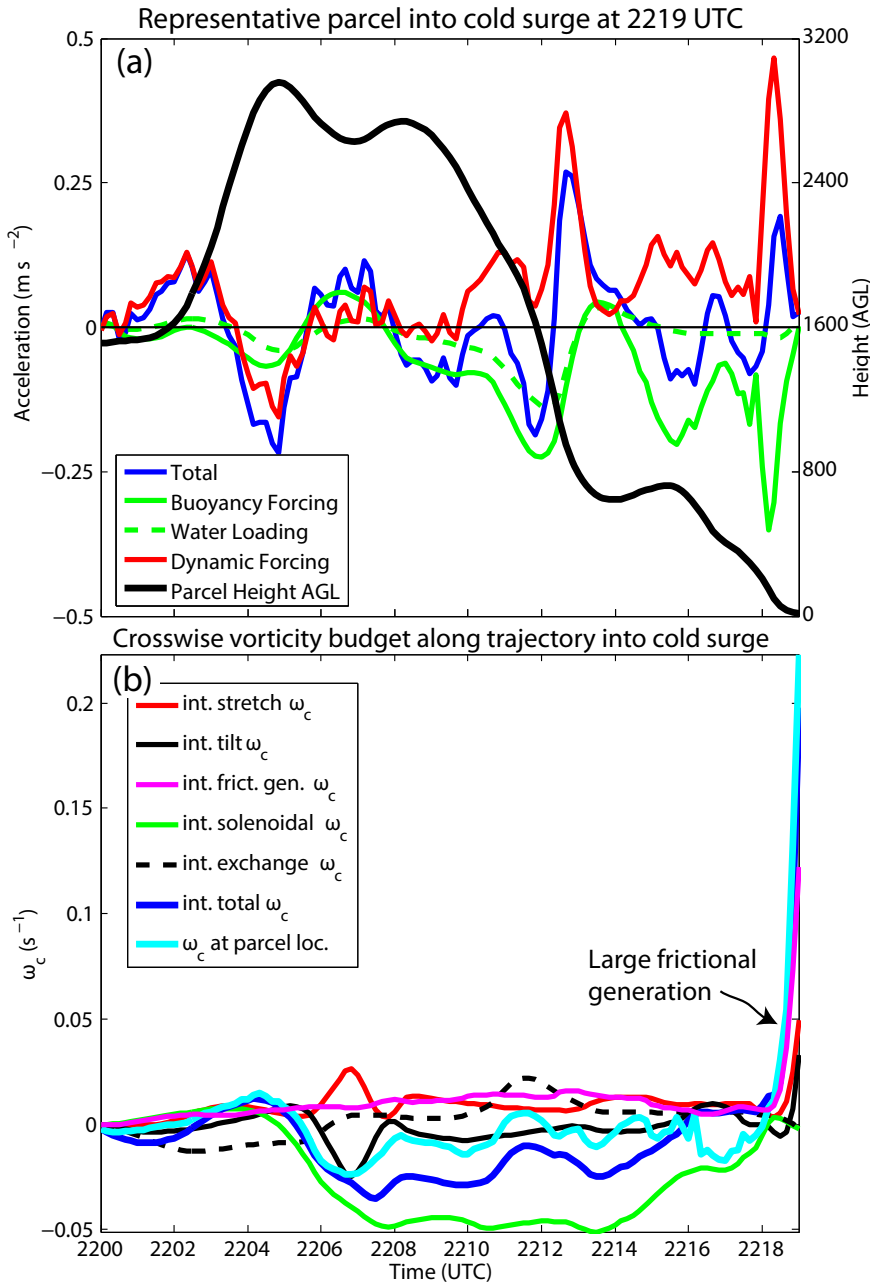


Fig. 15. (a) Forcing terms calculated along the representative trajectory in Fig. 14. The blue line is the sum of the effective buoyancy (green line) and dynamic forcing (red line). The black line is the trajectory height AGL. The dashed green line is the effective water loading term. (b) Crosswise vorticity equation terms integrated along the representative trajectory. Positive crosswise vorticity is defined as being to the left of parcel motion. The dark blue line is the sum of the integrated stretching (red line), baroclinic generation (green line), tilting (black line), exchange term (dashed black line), and frictional generation (magenta line). The cyan line is the Eulerian crosswise vorticity interpolated to the trajectory position from the model grid.